

A Giant Intragroup Nebula Hosting a Damped Ly α Absorber at z = 0.313

Hsiao-Wen Chen¹, Erin Boettcher¹, Sean D. Johnson^{2,3,5}, Fakhri S. Zahedy¹, Gwen C. Rudie³, Kathy L. Cooksey⁴, Michael Rauch³, and John S. Mulchaey

Department of Astronomy & Astrophysics, The University of Chicago, 5640 South Ellis Avenue, Chicago, IL 60637, USA; hchen@oddjob.uchicago.edu Department of Astrophysics, Princeton University, Princeton, NJ, USA

³ The Observatories of the Carnegie Institution for Science, 813 Santa Barbara Street, Pasadena, CA 91101, USA Department of Physics and Astronomy, University of Hawaii at Hilo, Hilo, HI 96720, USA Received 2019 April 28; revised 2019 May 20; accepted 2019 May 30; published 2019 June 17

Abstract

This Letter reports the discovery of spatially extended line-emitting nebula, reaching to ≈100 physical kpc (pkpc) from a damped Ly α absorber (DLA) at $z_{DLA} = 0.313$ along the sightline toward quasi-stellar object (QSO) PKS 1127–145 ($z_{\rm QSO}=1.188$). This DLA was known to be associated with a galaxy group of dynamical mass $M_{\rm group}\sim 3\times 10^{12}M_{\odot}$, but its physical origin remained ambiguous. New wide-field integral field observations revealed a giant nebula detected in [O II], H β , [O III], H α , and [N II] emission, with the line-emitting gas following closely the motions of group galaxies. One of the denser streams passes directly in front of the QSO with kinematics that are consistent with the absorption profiles recorded in the QSO echelle spectra. The emission morphology, kinematics, and line ratios of the nebula suggest that shocks and turbulent mixing layers, produced as a result of stripped gaseous streams moving at supersonic speed across the ambient hot medium, contribute significantly to the ionization of the gas. While the DLA may not be associated with any specific detected member of the group, both the kinematic and dust properties are consistent with the DLA originating in streams of gas stripped from sub- L_* group members at \lesssim 25 pkpc from the QSO sightline. This study demonstrates that gas stripping in low-mass galaxy groups is effective in releasing metal-enriched gas from star-forming regions, producing absorption systems in QSO spectra, and that combining absorption and emission-line observations provides an exciting new opportunity for studying gas and galaxy co-evolution.

Key words: galaxies: groups: individual (PKS 1127–145) – galaxies: halos – galaxies: interactions – galaxies: kinematics and dynamics

1. Introduction

The diffuse circumgalactic and intergalactic gas beyond visible galaxy disks contains >90% of all baryons in the universe (e.g., Miralda-Escudé et al. 1996; Fukugita 2004), serving as a reservoir of materials for sustaining the growth of galaxies while maintaining a record of feedback from previous episodes of star formation and active galactic nuclei (AGNs) activity. A comprehensive understanding of the origin and evolution of galaxies relies on accurate characterizations of this diffuse gas (e.g., Somerville & Davé 2015). However, direct imaging of the diffuse circumgalactic medium around distant galaxies has been challenging (e.g., Fynbo et al. 1999; Christensen et al. 2006; Rauch et al. 2008, 2011, 2013; Steidel et al. 2011; Krogager et al. 2017), because the gas density is typically too low to radiate at sufficiently high intensities (e.g., Cantalupo et al. 2005; Kollmeier et al. 2010) and because the factor of $(1+z)^4$ cosmological surface brightness dimming further suppresses the signal. On the other hand, quasar absorption spectroscopy has provided a sensitive probe of tenuous gas based on the absorption features imprinted in the quasar spectra (e.g., Rauch 1998; Wolfe et al. 2005; Chen 2017; Tumlinson et al. 2017).

Among different types of quasi-stellar object (QSO) absorption-line systems, damped Ly α absorbers (DLAs) with neutral hydrogen column density $N(\text{H I}) \geqslant 2 \times 10^{20} \, \text{cm}^{-2}$ are of particular significance in understanding the complex interface between star formation and the interstellar gas. The high N(H I) ensures that the gas is neutral which, together with the

presence of heavy elements, makes DLAs a promising signpost of distant galaxies. Studies of DLAs not only help characterize the cosmic evolution of neutral gas with time (e.g., Neeleman et al. 2016), but also provide key insights into the interplay between star formation in the instellar matter (ISM) of distant galaxies and their large-scale neutral gas properties (e.g., Wolfe et al. 2005).

Here we present a unique system, for which newly available wide-field integral field spectroscopic (IFS) data enabled detections of spatially extended line-emitting gas, connected directly to a previously known DLA at $z_{DLA} = 0.313$. It demonstrates the power of combining emission and absorption measurements, which provides a new and exciting opportunity for studying gas and galaxy co-evolution (compare Zhang et al. 2018). Throughout the Letter, we adopt a standard Λ cosmology, $\Omega_M=0.3$ and $\Omega_{\Lambda}=0.7$ with a Hubble constant $H_0=70\,{\rm km\,s}^{-1}\,{\rm Mpc}^{-1}$.

2. Observations and Data Descriptions

Here we briefly describe available imaging and spectroscopic data for characterizing the DLA and its surrounding gas and galaxy properties.

2.1. Galaxy Imaging and Spectroscopic Data

High spatial resolution optical images obtained using the Wide Field and Planetary Camera 2 (WFPC2) and the F814W filter on board the Hubble Space Telescope (HST) were retrieved from the HST data archive (PID = 9173; PI: Bechtold), and coadded to form a final combined image using

⁵ Hubble, Princeton–Carnegie fellow.

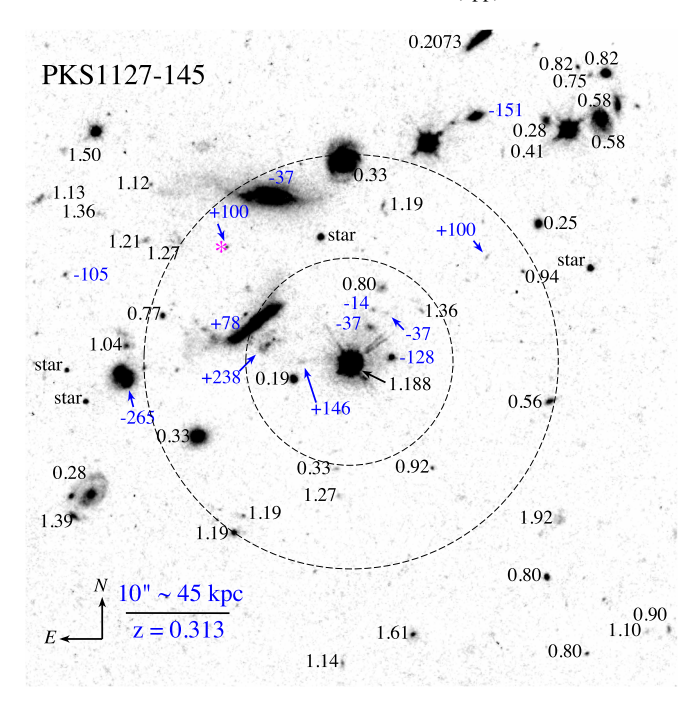


Figure 1. Summary of the redshift survey enabled by Multi-Unit Spectroscopic Explorer (MUSE) data. The image, obtained using *HST* WFPC2 and the F814W filter (PID = 9173), covers a sky area of $\approx 1' \times 1'$ centered at QSO PKS 1127–145 at $z_{\rm QSO}=1.188$. It reaches a 5σ limiting magnitude of *AB* (F814W) = 27.4 over a 0.75 diameter aperture. The dashed circles mark the 10" and 20" radii from the QSO sightline. Spectroscopically identified objects from the MUSE data are marked with redshift measurements. The redshifts of galaxies associated with the DLA at z=0.313 have been converted to line-of-sight velocity offsets from the fiducial redshift z=0.31266 (see Figure 2 below), which are shown in blue. The light-weighted center of the galaxy group, at (+12.72, +10.76) from the QSO, is marked by "*" in the image, corresponding to 74 physical kpc (pkpc) in projected distance (see the main text for details).

custom software. Source detection was performed using the SExtractor program (Bertin & Arnouts 1996). A portion of the combined image, covering the $\approx 1' \times 1'$ area centered at the QSO, is presented in Figure 1.

Wide-field IFS data of the field around PKS 1127-145 were obtained using the Multi-Unit Spectroscopic Explorer (MUSE; Bacon et al. 2010). MUSE observes a field of $1' \times 1'$ with a pixel scale of 0"2 and a spectral resolution of FWHM \approx 120 at 7000 Å. The observations were obtained under PID = 096.A-0303 (PI: Péroux), with a total integration of 8700 s and a mean seeing condition of FWHM $\approx 0.0^{\circ}$ 6. Pipeline-processed and flux-calibrated individual data cubes were downloaded from ESO Phase 3 data archive. The individual data cubes were combined using custom software with optimal weights determined based on the inverse variance of the sky and with the world coordinates calibrated to match the HST WFPC2 image. The wavelength array was converted to vacuum. Finally, a median sky spectrum was formed using spaxels in blank areas and subtracted from the final combined data cube to reduce sky residuals.

The combined MUSE data cube reaches a 1σ limiting sensitivity over a 1'' box of $1.7 \times 10^{-19}\,\mathrm{erg\,s^{-1}\,cm^{-2}\,\mathring{A}^{-1}\,arcsec^{-2}}$ at 4900 and 8600 \mathring{A} , and $8 \times 10^{-20}\,\mathrm{erg\,s^{-1}\,cm^{-2}\,\mathring{A}^{-1}\,arcsec^{-2}}$ at 6600 \mathring{A} . It enables a highly complete spectroscopic survey of faint galaxies in the QSO field, including those in the vicinity of the DLA at $z_{\mathrm{DLA}}=0.313$. We extracted object spectra from the final

MUSE data cube using a circular aperture of two pixels (0."4) in radius. Redshift measurements were based on a χ^2 fitting routine described in Chen & Mulchaey (2009) and Johnson et al. (2013). The best-fit redshift of each object was visually inspected for confirmation. This exercise led to robust redshift measurements of 63 objects, 13 of which are found within 30" of the DLA. The redshift measurements are presented in Figure 1. To avoid crowding, redshifts of galaxies not associated with the DLA are presented to two decimal places. For the galaxies associated with the DLA, the line-of-sight velocity offsets are shown relative to z = 0.31266 (see below).

2.2. Absorption Spectra of the QSO

Absorption spectra of PKS 1127–145 were obtained using the Faint Object Spectrograph and the low-resolution G160L grating on board *HST* (PID = 6577; PI: Rao), the Space Telescope Imaging Spectrograph (STIS) and the E230M grating (PID = 9173; PI: Bechtold), and the Ultraviolet and Visual Echelle Spectrograph (UVES; D'Odorico et al. 2000) on the Very Large Telescope (VLT)-UT2 telescope under multiple programs (67.A-0567, 69.A-0371, 076.A-086). Details regarding the STIS and UVES data processing are described in Cooksey et al. (2010) and Zahedy et al. (2017), respectively.

These ultraviolet and optical spectra enabled detailed studies of the chemical and dust content of the DLA (e.g., Kanekar et al. 2014; Guber et al. 2018). In particular, the high-resolution echelle spectra provide the wavelength coverage for observing a suite of heavy ions, including Mg⁺, Fe⁺, Mn⁺, Ti⁺, and Ca⁺. A summary of the absorption properties of the DLA is presented in Figure 2. Metal absorption lines, such as Mn II, Ti II, and Ca II, are resolved into at least six individual components. The strongest Mn II component occurs at $z_c = 0.31266$, which is adopted as the redshift zero-point for subsequent discussions. The remaining components are detected at relative line-of-sight velocities, $\Delta v_c = -36$, +15, +27, +46, and +76 km s⁻¹ (vertical dotted lines in Figure 2).

3. The Galactic Environment of the DLA at $z_{DLA} = 0.313$

The MUSE observations described in Section 2.1 have yielded a total of 13 galaxies in the vicinity of the DLA at $z_{\rm DLA} = 0.313$ toward PKS 1127–145 (see Péroux et al. 2019), with redshifts ranging from z = 0.3115 to z = 0.3137 and physical projected distances from d = 17.4 physical kpc (pkpc) to d = 130 pkpc. Including the galaxy found at z = 0.3124 and d = 241 kpc by Kacprzak et al. (2010), we establish a total of 14 galaxies associated with the DLA, four of which are new from this work (see Kacprzak et al. 2010; Péroux et al. 2019). Table 1 presents a complete list of galaxies spectroscopically identified in the vicinity of the DLA. In columns (1) through (11), we present the galaxy ID based on their J2000 coordinates, best-fit redshift, angular offsets in R.A. and decl. $(\Delta \alpha, \Delta \delta)$ and angular distance (θ) of the galaxy from the background QSO, the projected distance (d) in physical units from the QSO sightline, the line-of-sight velocity offset from the fiducial redshift $z = 0.31266 \ (\Delta v_g)$, the observed AB (F814W) magnitude, the corresponding rest-frame r-band absolute magnitude (M_r) , the intrinsic luminosity in units of L_* , and cross-reference ID from Kacprzak et al. (2010) and Péroux et al. (2019).6

⁶ Note that G20 was identified by Péroux et al. (2019) as a group member based on the absorption features, but we find it to be a star.

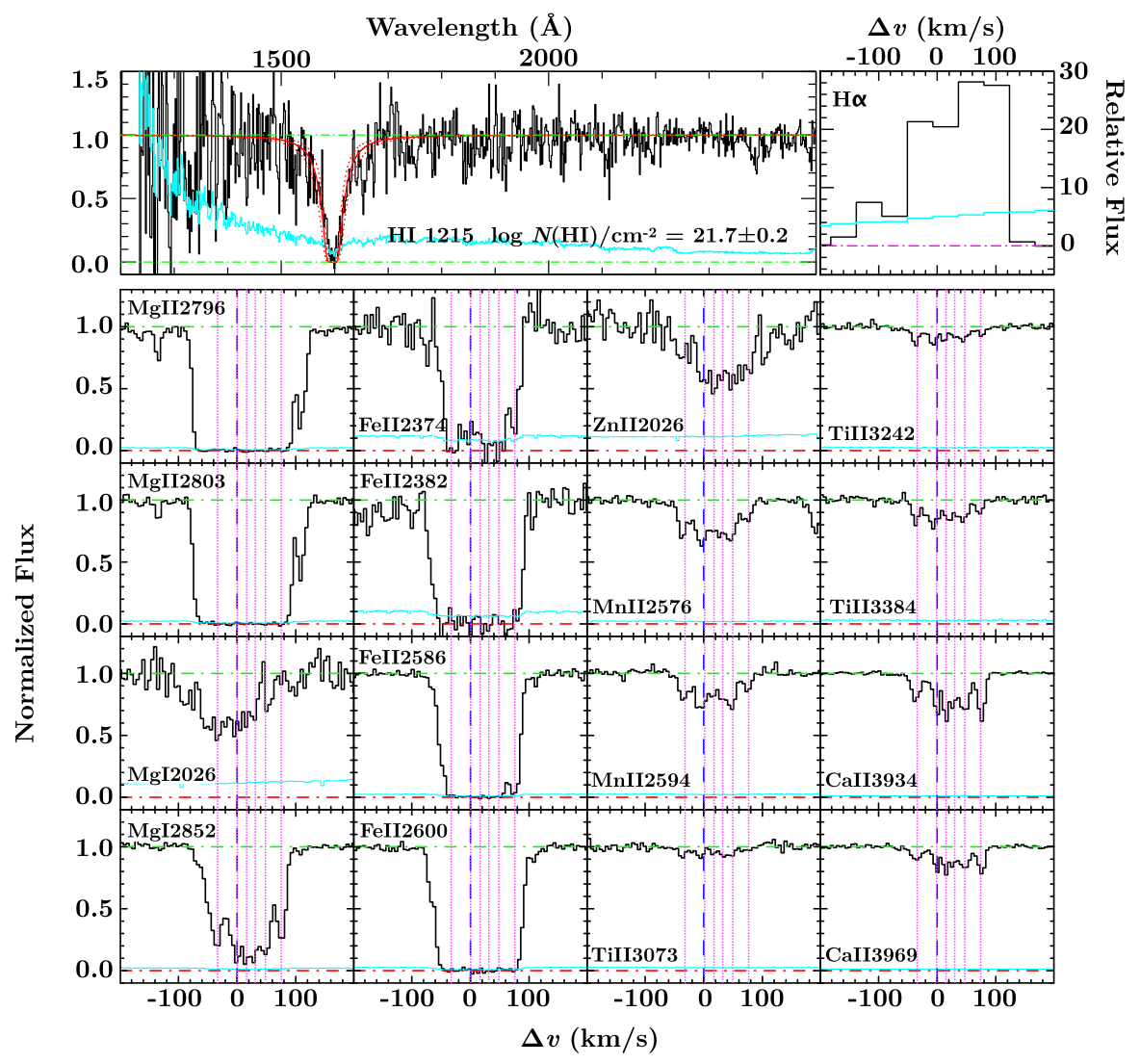


Figure 2. Comparison of gas kinematics in emission and in absorption. The top-left panel displays the continuum-normalized HST Faint Object Spectrograph spectrum in black, and the associated 1σ error spectrum in cyan. The strong absorption at ≈ 1500 Å is the hydrogen $Ly\alpha$ absorption feature with the best-fit Voigt profiles of $\log N(\rm H~I)/\rm cm^{-2} = 21.7 \pm 0.2$ (shown in red; see also Rao & Turnshek 2000). The bottom panels display metal absorption lines associated with the DLA from UVES and STIS observations. Zero velocity corresponds to z = 0.31266. While strong transitions such as Mg II and Fe II are saturated, unsaturated transitions such as Mg I, Mn II, Ti II, and Ca II are well resolved into six individual components (vertical dotted lines; see also Guber et al. 2018). For comparison, the $H\alpha$ line from the line-emitting gas at 1.75 east of the QSO sightline is shown in the upper-right panel. While the emission spectrum does not have a sufficient spectral resolution for resolving small-scale motions, both the velocity centroid and width of the emission from the gaseous stream near the QSO sightline agree well with the mean and dispersion of the absorbing components.

The galaxy group in the vicinity of the DLA spans a range in the optical brightness, from $AB(\text{F}814\text{W}) \approx 19$ to $AB(\text{F}814\text{W}) \approx 25.2$ mag. At z=0.313, the observed F814W band corresponds to the rest-frame r-band. The observed brightnesses therefore translate directly to the rest-frame r-band luminosities. Adopting the characteristic rest-frame absolute r-band magnitude of $M_{r_*}=-21.3$ for blue galaxies from Cool et al. (2012), the corresponding rest-frame luminosities range from $\lesssim 0.01\,L_*$ to $\approx 1.6\,L_*$ (see also Kacprzak et al. 2010; Péroux et al. 2019). In addition, the observed line-of-sight velocity offsets of the group members relative to the strongest absorption component at z=0.31266 range from $\Delta v_g=-265$ to $\Delta v_g=+238\,\mathrm{km}\,\mathrm{s}^{-1}$.

We also compute the light-weighted center of the group at $(+12\rlap.{''}2, +10\rlap.{''}6)$ from the QSO (marked by "*" in Figure 1), with a corresponding projected distance of $d_{\rm group}=74\,{\rm pkpc}$ from the DLA. The observed line-of-sight velocity dispersion

of $\sigma_{\rm v}=128\,{\rm km~s^{-1}}$ among the 14 group members indicates a dynamical group mass of $M_{\rm group}\sim3\,\times\,10^{12}\,M_{\odot}$.

The presence of a galaxy group around the DLA complicates common theories of the physical origin of the high-column density gas. With a mean gas metallicity $5 \times$ lower in the DLA than in the ISM of luminous group members, previously favored scenarios include low-luminosity dwarf satellites (e.g., York et al. 1986), tidal debris in the group environment (e.g., Kacprzak et al. 2010), and diffuse intragroup medium (e.g., Péroux et al. 2019).

However, in addition to individual galaxies associated with DLA, the MUSE data also uncovered spatially extended line-emitting gas, detected in $H\alpha$, $H\beta$, [O III], and [O II], across the galaxy group. The emitting morphology is consistent with the gas being stripped from members of the galaxy group, which is similar to what was found in other group environments (e.g., Epinat et al. 2018; Johnson et al. 2018). One of the denser

Table 1 Galaxy Properties in the Vicinity of the DLA at z = 0.313

		$\Delta \alpha$	$\Delta \delta$	θ	d	$\Delta v_g^{\ a}$	<i>AB</i> (F814W)	$M_r^{\ b}$	L_r		
ID	z	(")	(")	(")	(pkpc)	(km s^{-1})	(mag)	(mag)	(L_*)	Type ^c	crossID ^d
(1)	(2)	(3)	(4)	(5)	(6)	(7)	(8)	(9)	(10)	(11)	(12)
J113006.80-144926.86	0.3121	-3.8	+0.4	3.8	17.4	-128	22.11	-18.66	0.09	em	G1
J113006.92-144923.96	0.3125	-2.0	+3.3	3.9	17.9	-37	22.19	-18.58	0.08	abs	
J113007.38-144927.06	0.3133	+4.6	+0.2	4.6	21.3	+146	24.56	-16.21	0.01	em	G16
J113006.89-144922.36	0.3126	-2.5	+4.9	5.5	25.3	-14	23.88	-16.89	0.02	em	
J113006.82-144922.63	0.3125	-3.5	+4.7	5.8	26.7	-37	24.67	-16.10	0.01	em	G18
J113007.61-144925.49	0.3137	+8.0	+1.8	8.2	37.5	+238	21.79	-18.98	0.12	em	G17
J113007.68-144923.29	0.3130	+9.0	+4.0	9.8	45.1	+78	19.24	-21.53	1.24	em	G2
J113007.86-144916.36	0.3131	+11.6	+10.9	15.9	73.1	+100	25.18	-15.59	0.01	em	
J113006.16-144917.16	0.3131	-13.1	+10.1	16.5	75.8	+100	25.15	-15.62	0.01	em	
J113007.58-144911.01	0.3125	+7.5	+16.3	17.9	82.2	-37	18.95	-21.82	1.62	LINER	G4
J113008.55-144928.26	0.3115	+21.6	-1.0	21.6	98.8	-265	20.20	-20.57	0.51	em	G6
J113006.23-144903.80	0.3120	-12.0	+23.5	26.4	120.8	-151	21.32	-19.45	0.18	em	G19
J113008.92-144918.30	0.3122	+27.0	+9.0	28.4	130.1	-105	24.51	-16.26	0.01	em	G21
J113010.32-144904.34	0.3124 ^e	+47.3	+23.0	52.5	240.6	-59	20.42	-20.35	0.42	em	G14

Notes

streams passes directly in front of the QSO with kinematics consistent with the absorption profiles revealed in the QSO echelle spectrum. While the MUSE data do not have the spectral resolution necessary to resolve relative motions under $\approx 100 \, \mathrm{km \ s^{-1}}$, both the velocity centroid and width of the lines near the QSO sightline agree well with the mean and dispersion of the absorbing components (top-right panel in Figure 2). The imaging panels in Figure 3 compare the spatial distributions of the stellar continuum revealed in the HST F814W image and the line-emitting nebula from the MUSE data. Continuum subtracted line-flux maps of $[O II]\lambda\lambda3727$, 3729, $[O III]\lambda5007$, and $H\alpha$ integrated over a velocity window from $\Delta v = -200 \,\mathrm{km \, s^{-1}}$ to $\Delta v = +250 \,\mathrm{km \, s^{-1}}$ are displayed. The line-emitting gas, detected in multiple transitions, is seen to extend much beyond the stellar disks, reaching to ≈ 100 pkpc from the QSO sightline.

In addition, this extended gas is seen to follow a coherent motion that closely traces the motion of the galaxies in the group, with the intensity peaks moving from $\approx -200 \, \mathrm{km \, s^{-1}}$ west to $\approx +250 \, \mathrm{km \, s^{-1}}$ east of the QSO (*left* panels of Figure 4). Furthermore, the gas exhibits a broad range in velocity dispersion. The observed large dispersion in [O III], in particular, indicates the presence of turbulent, multiphase intragroup gas (see Johnson et al. 2018 see below). We measure a total integrated line flux in $\mathrm{H}\alpha$ of $f(\mathrm{H}\alpha) = (1.38 \pm 0.01) \times 10^{-15} \, \mathrm{erg \, s^{-1} \, cm^{-2}}$ and in [O III] of $f(\mathrm{[O III]}) = (8.06 \pm 0.05) \times 10^{-16} \, \mathrm{erg \, s^{-1} \, cm^{-2}}$.

4. Discussion

Newly available wide-field IFS observations of the field around PKS 1127–145 have provided a wealth of information concerning the galactic environment of the DLA at $z_{\rm DLA} = 0.313$. While this DLA is previously known to be associated with a galaxy group (e.g., Bergeron & Boissé 1991; Chen & Lanzetta 2003; Kacprzak et al. 2010; Péroux et al. 2019), the IFS data have uncovered spatially extended, line-

emitting nebula connecting between members of the galaxy group. One of the denser streams passes directly in front of the QSO with kinematics consistent with the absorption profiles revealed in the QSO echelle spectrum, establishing a direct connection between the DLA and the giant nebula.

The MUSE data also allow us to examine the physical condition of the gas based on comparisons of multiple transitions. First, we examine the gas density based on the observed [O II] doublet ratio and the H\$\alpha\$ surface brightness (e.g., Osterbrock & Ferland 2006). The [O II] \$\lambda3729 line is found to be comparable or stronger than the \$\lambda3727 member across the line-emitting nebulae, constraining the electron density at $n_e \lesssim 300 \, \mathrm{cm}^{-3}$. At the same time, the observed H\$\alpha\$ surface brightness is related to the gas density following,

$$SB_{H\alpha} \approx 1.7 \times 10^{-15} C \frac{\langle n_e \rangle^2}{(1+z)^4}$$
$$\times \frac{l_{\text{neb}}}{\text{kpc}} \text{ erg s}^{-1} \text{ cm}^{-2} \text{ arcsec}^{-2}, \tag{1}$$

where $C \equiv \langle n_e^2 \rangle / \langle n_e \rangle^2$ represents the clumping factor of the line-emitting gas, $\langle n_e \rangle$ represents the mean gas density, and $l_{\rm neb}$ represents the depth of the line-emitting region in units of kpc. Adopting a characteristic surface brightness of $2.5 \times 10^{-17} \, {\rm erg \, s^{-1} \, cm^{-2} \, arcsec^{-2}}$ from Figure 3 and assuming $l_{\rm neb} = 1 \, {\rm kpc}$ leads to a crude estimate of gas density of $\langle n_e \rangle = 0.2(0.06) \, {\rm cm^{-3}}$ for C = 1(10).

Next, we examine the ionization state of the gas by measuring the $[O III]\lambda 5007/[O II]\lambda \lambda 3727$, 3729 ratio in the nebula. Panel (e) of Figure 4 shows the contours of [O III]/[O II] = 1/3 (cyan) and 1 (magenta). These contours identify the locations of highly ionized gas both within 45 pkpc of the DLA and next to the two super- L_* spirals in the group with flared/warped disk morphologies. Because the observed [O III]/[O II] ratio depends on both the ionization radiation and gas metallicity (e.g., Kewley & Dopita 2002), we also

^a $\Delta v_g = 0$ corresponds to z = 0.31266, the strongest absorbing component in Figure 2.

^b We adopt a characteristic rest-frame absolute r-band magnitude of $M_{r_*} = -21.3$ from Cool et al. (2012).

^c Spectral type of the galaxy: emission-line ("em"), absorption ("abs"), or low-ionization nuclear emission-line region (LINER) dominated.

^d Galaxy IDs from Kacprzak et al. (2010) and Péroux et al. (2019).

e This galaxy occurs outside the MUSE field of view. Redshift is taken from Kacprzak et al. (2010).

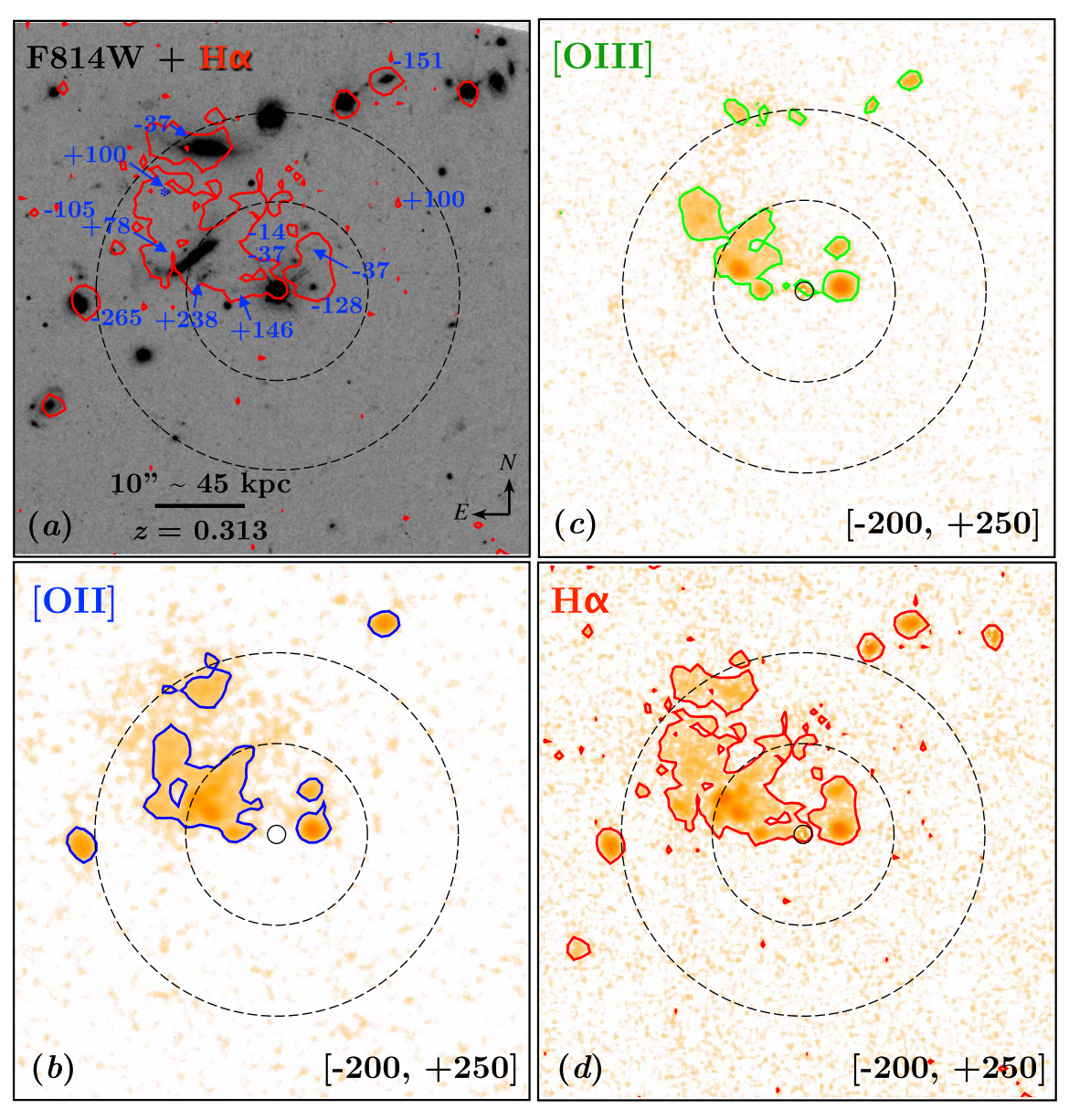


Figure 3. Spatial distribution of line-emitting gas relative to the stellar continuum. Panel (a) shows the *HST* F814W image of the field around PKS 1127–145 with spectroscopically identified galaxy group members marked by their line-of-sight velocity offsets. The continuum subtracted line-flux maps of [O III] $\lambda\lambda$ 3727, 3729, [O III] λ 5007, and H α integrated over a velocity window from $\Delta \nu = -200 \, \mathrm{km \, s^{-1}}$ to $\Delta \nu = +250 \, \mathrm{km \, s^{-1}}$ are displayed in panels (b)–(d) with the contours representing the constant surface brightness of 2.5 × 10⁻¹⁷ erg s⁻¹ cm⁻² arcsec⁻². The H α contour from panel (d) is superimposed on the F814W image in panel (a) to highlight that the line-emitting gas extends much beyond the stellar disks.

place this gas on the Baldwin, Phillips & Terlevich (BPT) diagram (Baldwin et al. 1981) to examine how the observed $[O III]\lambda5007/H\beta$ compares with $[N II]\lambda6585/H\alpha$ (e.g., Kewley et al. 2013).

Panel (f) of Figure 4 shows line ratios at different locations in the nebula, in comparison to the ISM of the group galaxies. Error bars show the 1σ measurement uncertainties. While the galaxies appear to be typical of distant star-forming galaxies on the BPT diagram, the observed line ratios of high [O III]/[O II] regions appear in the parameter space traditionally occupied by active galaxies, indicating the need of a hard ionizing spectrum to account for the ionization condition of the gas (e.g., Kewley

et al. 2013). Specifically, the nebula at >10'' (>45 pkpc) from the QSO sightline (regions *B* and *C* in Panel (e) of Figure 4) appears to be under a more extreme ionizing condition than the gas closer to the QSO sightline.

Possible sources for a hard radiation field include AGN, turbulent mixing layers (e.g., Slavin et al. 1993; Miller & Veilleux 2003), and shocks (e.g., Dopita & Sutherland 1995; Rich et al. 2011). We have searched for signatures of AGN in the group galaxies by examining their optical spectra and WISE photometry (e.g., Wright et al. 2010; Mateos et al. 2013), and found none. The spatial variation of the ionization state of the gas is also inconsistent with fossil ionized regions from a previous AGN outburst. On the other hand, the presence of extended stellar streams from the two super- L_* disk galaxies in the HST image are indicative of ongoing violent galaxy interactions between the group members. For a dynamical mass

 $^{^{7}}$ Note that J113007.58–144911.01 (G4 in Péroux et al. 2019) at 82 pkpc exhibits a LINER-like [N II]/H α but is not detected in H β or [O III], preventing its inclusion in the panel.

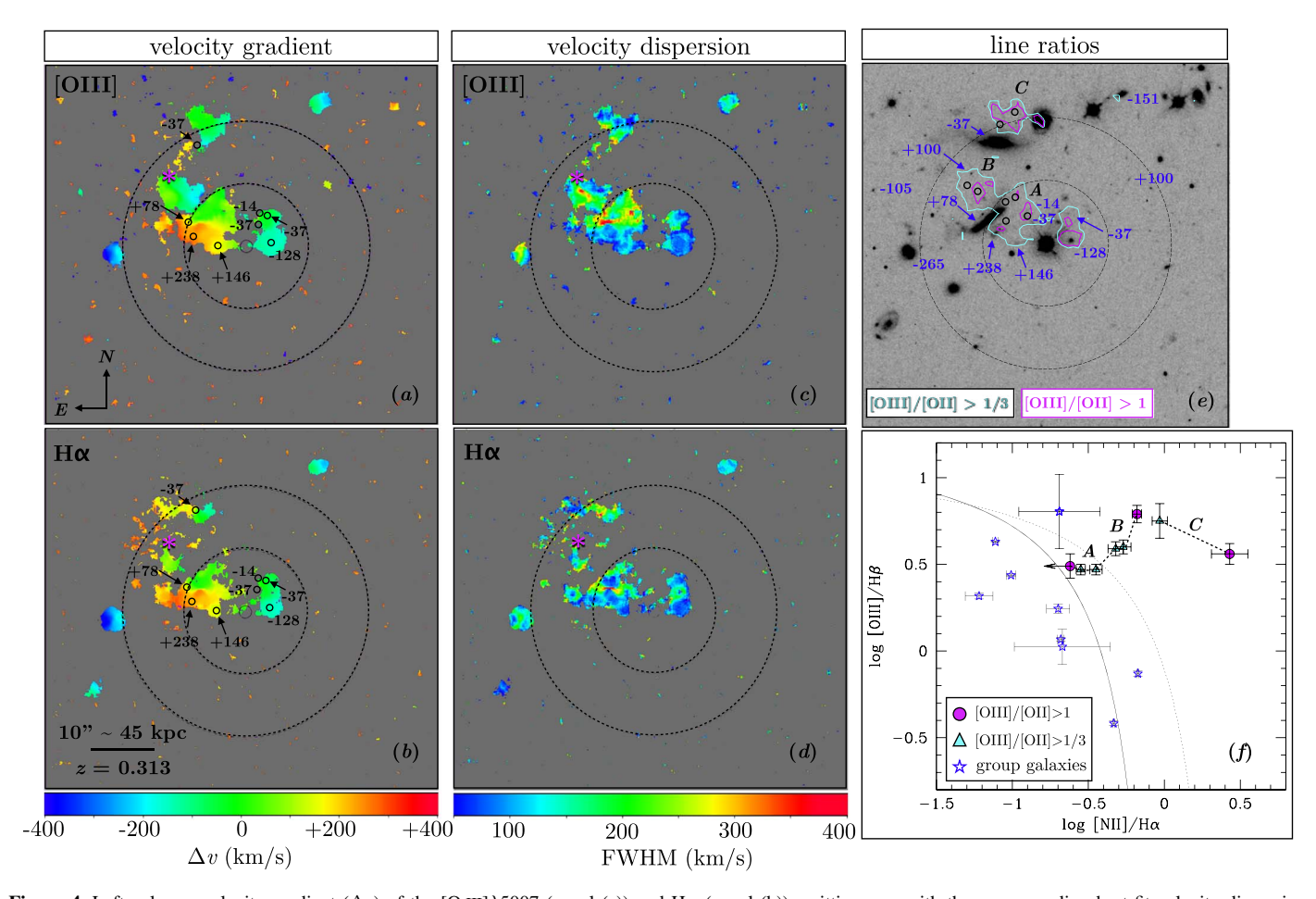


Figure 4. Left column: velocity gradient (Δv) of the $[O III]\lambda 5007$ (panel (a)) and $H\alpha$ (panel (b)) emitting gas, with the corresponding best-fit velocity dispersion (FWHM in km s⁻¹), after removing the instrument line width, displayed in panels (c) and (d), respectively, in the middle column. Zero velocity corresponds to z=0.31266. The positions of the galaxies that coincide with the nebula are marked by open circles along with their line-of-sight velocity offsets, showing that the line-emitting gas following closely the motions of group galaxies. Panel (e) highlights the locations where [O III]/[O II] > 1/3 (cyan contours) and >1 (magenta contours), relative to group galaxies. Panel (f) shows the observed $[O III]\lambda 5007/H\beta$ vs. $[N II]\lambda 6585/H\alpha$ ratios for three regions, A, B, and C, in Panel (e), at angular distances of <10'', between 10'' and >20'', respectively. The measurements are made based on integrated line fluxes over a 1''-diameter aperture, and the positions of the apertures are marked by open circles in Panel (e). For comparison, the line ratios observed in the ISM of the group galaxies are also included. Error bars represent the 1σ measurement uncertainties. The solid and dotted curves are from Kauffmann et al. (2003) and Kewley et al. (2001), respectively, separating star-forming regions (lower left) from active galaxies (upper right).

of $M_{\rm group}\sim 3\times 10^{12}\,M_{\odot}$, the temperature of the intragroup medium would be $T\sim 2\times 10^6$ K, if present, and the sound speed of the hot halo would be $c_s \sim 220 \, \mathrm{km \ s^{-1}}$. As galaxies move through this hot intragroup medium, ram-pressure stripping, in addition to tidal interactions between galaxy group members, is expected to be effective in removing the ISM (e.g., Gunn & Gott 1972; Roediger & Brüggen 2007) and shocks and/or turbulent mixing layers should form as stripped gaseous streams travel through the hot gas at supersonic speed. Both the observed line widths seen in [O III] and H α (panels (c) and (d)) and emission morphologies are consistent with the expectation that the line-emitting gas originates in shocks or turbulent mixing layers. Ram-pressure and tidal stripping are most effective in removing gas in the outskirts of galaxies (e.g., Roediger & Brüggen 2007). Coupled with metallicity gradients commonly seen in galaxy disks (e.g., Bresolin 2017), this naturally explains the low metallicity in the DLA.

In summary, available MUSE data have revealed a complex, multiphase intragroup medium hosting a DLA at $z_{\rm DLA} = 0.313$. The DLA is not associated with any specific detected member of the group. Both the kinematic and dust properties are consistent with the absorber originating in

streams of stripped gas from sub- L_* group members at $d \lesssim 25$ pkpc from the QSO sightline as a result of violent interactions in the group environment. In contrast, the nebula at d > 45 pkpc likely originates in the two super- L_* spirals; and its kinematics, line ratios, and morphologies are consistent with being ionized by shocks or turbulent mixing layers. This system demonstrates that metal-enriched gas can be released from star-forming regions into the intragroup medium through effective gas stripping processes in distant low-mass groups, where it produces absorption systems in QSO spectra.

We thank the anonymous referee, as well as Céline Péroux and Don York for helpful comments on an earlier draft. H.W. C., E.B., and F.S.Z. acknowledge partial support from NSF AST-1715692 and *HST*-GO-15163.01A grants. S.D.J. acknowledges support by NASA through a Hubble Fellowship grant *HST*-HF2-51375.001-A. K.L.C. acknowledges support from NSF grant AST-1615296.

Software: SExtractor (Bertin & Arnouts 1996).

ORCID iDs

Hsiao-Wen Chen https://orcid.org/0000-0001-8813-4182 Erin Boettcher https://orcid.org/0000-0003-3244-0409

References

```
Bacon, R., Accardo, M., Adjali, L., et al. 2010, Proc. SPIE, 7735, 773508
Baldwin, J. A., Phillips, M. M., & Terlevich, R. 1981, PASP, 93, 5
Bergeron, J., & Boissé, P. 1991, A&A, 234, 344
Bertin, E., & Arnouts, S. 1996, A&AS, 117, 393
Bresolin, F. 2017, in Outskirts of Galaxies, ed. J. H. Knapen, J. C. Lee, &
   A. Gil de Paz (Berlin: Springer), 145
Cantalupo, S., Porciani, C., Lilly, S. J., & Miniati, F. 2005, ApJ, 628, 61
Chen, H.-W. 2017, in Outskirts of Galaxies, ed. J. H. Knapen, J. C. Lee, &
   A. Gil de Paz (Berlin: Springer), 291
Chen, H.-W., & Lanzetta, K. M. 2003, ApJ, 597, 706
Chen, H.-W., & Mulchaey, J. S. 2009, ApJ, 701, 1219
Christensen, L., Wisotzki, L., Roth, M. M., et al. 2006, A&A, 468, 587
Cooksey, K. L., Thom, C., Prochaska, J. X., & Chen, H. 2010, ApJ, 708, 868
Cool, R. J., Eisenstein, D. J., Kochanek, C. S., et al. 2012, ApJ, 748, 10
D'Odorico, S., Cristiani, S., Dekker, H., et al. 2000, Proc. SPIE, 4005, 121
Dopita, M. A., & Sutherland, R. S. 1995, ApJ, 455, 468
Epinat, B., Contini, T., Finley, H., et al. 2018, A&A, 609, A40
Fukugita, M. 2004, in Proc. IAU Symp. 220, Dark Matter in Galaxies, ed.
   S. Ryder et al. (San Francisco, CA: ASP), 227
Fynbo, J. U., Møller, P., & Warren, S. J. 1999, MNRAS, 305, 849
Guber, C. R., Richter, P., & Wendt, M. 2018, A&A, 609, A85
Gunn, J.-E., & Gott, J. R., III 1972, ApJ, 176, 1
Johnson, S. D., Chen, H.-W., & Mulchaey, J. S. 2013, MNRAS, 434, 1765
Johnson, S. D., Chen, H.-W., Straka, L. A., et al. 2018, ApJL, L1
Kacprzak, G. G., Murphy, M. T., & Churchill, C. W. 2010, MNRAS, 406, 445
Kanekar, N., Prochaska, J. X., Smette, A., et al. 2014, MNRAS, 438, 2131
```

```
Kauffmann, G., Heckman, T. M., Tremonti, C., et al. 2003, MNRAS,
  346, 1055
Kewley, L. J., & Dopita, M. A. 2002, ApJS, 142, 35
Kewley, L. J., Dopita, M. A., Leitherer, C., et al. 2013, ApJS, 774, 100
Kewley, L. J., Dopita, M. A., Sutherland, R. S., Heisler, C. A., & Trevena, J.
  2001, ApJ, 556, 121
Kollmeier, J. A., Zheng, Z., Davé, R., et al. 2010, ApJ, 708, 1048
Krogager, J.-K., Møller, P., Fynbo, J. P. U., & Noterdaeme, P. 2017, MNRAS,
   469, 2959
Mateos, S., Alonso-Herrero, A., Carrera, F. J., et al. 2013, MNRAS, 434, 941
Miller, S. T., & Veilleux, S. 2003, ApJ, 592, 79
Miralda-Escudé, J., Cen, R., Ostriker, J. P., & Rauch, M. 1996, ApJ, 471, 582
Neeleman, M., Prochaska, J. X., Ribaudo, J., et al. 2016, ApJ, 818, 113
Osterbrock, D. E., & Ferland, G. J. 2006, Astrophysics of Gaseous Nebulae
  and Active Galactic Nuclei (Sausalito, CA: University Science Books)
Péroux, C., Zwaan, M. A., Klitsch, A., et al. 2019, MNRAS, 485, 1595
Rao, S. M., & Turnshek, D. A. 2000, ApJS, 130, 1
Rauch, M. 1998, ARA&A, 36, 267
Rauch, M., Becker, G. D., Haehnelt, M. G., Gauthier, J.-R., &
  Sargent, W. L. W. 2013, MNRAS, 429, 429
Rauch, M., Becker, G. D., Haehnelt, M. G., et al. 2011, MNRAS, 418, 1115
Rauch, M., Haehnelt, M., Bunker, A., et al. 2008, ApJ, 681, 856
Rich, J. A., Kewley, L. J., & Dopita, M. A. 2011, ApJ, 734, 87
Roediger, E., & Brüggen, M. 2007, MNRAS, 380, 1399
Slavin, J. D., Shull, J. M., & Begelman, M. C. 1993, ApJ, 407, 83
Somerville, R. S., & Davé, R. 2015, ARA&A, 53, 51
Steidel, C. C., Bogosavljević, M., Shapley, A. E., et al. 2011, ApJ, 736, 160
Tumlinson, J., Peeples, M. S., & Werk, J. K. 2017, ARA&A, 55, 389
Wolfe, A. M., Gawiser, E., & Prochaska, J. X. 2005, ARA&A, 43, 861
Wright, E. L., Eisenhardt, P. R. M., Mainzer, A. K., et al. 2010, AJ, 140, 1868
York, D., Dopita, M., Green, R., & Bechtold, J. 1986, ApJ, 311, 610
Zahedy, F. S., Chen, H.-W., Gauthier, J.-R., & Rauch, M. 2017, MNRAS,
  466, 1071
Zhang, H., Zaritsky, D., Werk, J., & Behroozi, P. 2018, ApJL, 866, L4
```